NiCo$_2$N nanosheets catalyzed peroxymonosulfate activation to generate ^{1}O$_2$ and SO$_4^{\bullet-}$ for efficient pollutant degradation: The role of nitrogen atoms

Pengcheng Cai [a],[1], Xiaohui Zhang [a],[1], Shuai Yang [b], Hui Cui [a], Yonghao Wang [a], Yaqi Huang [a], Mengjie Qin [a], Dandan Han [c], Xianfeng Yang [d], Peng Guo [e], Yuanyuan Sun [a],*, Dongjiang Yang [a],*

[a] School of Environmental Science and Engineering, State Key Laboratory of Bio-fibers and Eco-textiles, Shandong Collaborative Innovation Center of Marine Bio-based Fibers and Ecological Textiles, Qingdao University, Qingdao 266071, PR China
[b] School of Physical Science and Technology, Shanghai Tech University, Shanghai 201210, PR China
[c] School of Chemistry and Chemical Engineering, Heze University, Heze, PR China
[d] Analytical and Testing Centre, South China University of Technology, Guangzhou 510640, PR China
[e] Advanced Chemical Engineering and Energy Materials Research Center, China University of Petroleum (East China), Qingdao 266580, PR China

A R T I C L E   I N F O

A B S T R A C T

Advanced heterogeneous catalysts are essential for enhancing peroxymonosulfate (PMS) activation. Herein, a novel and highly highly-efficient PMS activation catalyst, NiCo$_2$N nanosheets (NiCo$_2$N NS), is reported. Owing to the strong electron transfer ability of Ni-N and Co-N, the NiCo$_2$N NS/PMS system exhibit outstanding degradation performance and high cycling stability (100 % degradation after four cycles). The Co 3d orbital electrons in NiCo$_2$N are closer to the to the Fermi level than that in NiCo$_2$O$_4$ NS, resulting in its higher chemical reactivity with PMS. When PMS is adsorbed onto Ni-N and Co-N sites through a "bridge" mode, the O-O bond is broken instantaneously to generate SO$_4^{\bullet-}$ and HO*. The formed HO* is then deprotonated to O*, followed by a reaction with another O* to generate ^{1}O$_2$. This study reports the first use of transition-metal nitride as a heterogeneous catalyst in PMS activation and provides insights into the key role of N atoms.

1. Introduction

Advanced oxidation process (AOP) based on sulfate radical (SO$_4^{\bullet-}$) is an efficient and convenient method for degrading contaminants [1–3]. Besides comparable oxidation capability (2.5–3.1 V vs standard hydrogen electrode), SO$_4^{\bullet-}$ possess a longer half-life (30–40 µs) than $^\bullet$OH (20 ns). Thus, SO$_4^{\bullet-}$ can travel longer distances than $^\bullet$OH and encounter more target pollutants, enhancing the degradation performance. SO$_4^{\bullet-}$ is generated by persulfate activation. Compared to peroxydisulfate (PDS), peroxymonosulfate (PMS) can be activated more easily because of its asymmetric structure [4,5]. Thus, the activation of PMS to degrade pollutants has become a popular research topic [6,7]. Some PMS activation approaches, such as photocatalysis, electrolysis, heating, and ultrasound, require excess energy consumption and complex operation. The commonly applied carbonaceous-based catalysts suffer from high carbonization temperature (~ 800 °C), possible carbon release to water, and poor recyclability because of the adsorption coverage of the active sites. Therefore, many efforts have been made to develop more effective

and practicable catalysts to produce SO$_4^{\bullet-}$ for pollutant degradation and environmental remediation.

Heterogeneous Co-mediated PMS activation strategy has been extensively studied since Anipsitakis and Dionysiou [8] reported that Co (II) has excellent PMS activation activity in homogeneous reactions. The versatile Co$_3$O$_4$ has attracted significant attention because of its stability and facile synthesis. The generation of SO$_4^{\bullet-}$ is accompanied by the electron transfer from ≡Co(II) to PMS. To complete the catalytic cycle, ≡Co(III) is further reduced by another PMS molecule. Furthermore, the introduction of another metal into Co$_3$O$_4$ to partially substitute the Co atom has a crucial influence on the catalytic performance. In particular, doping nickel into Co$_3$O$_4$ to form bimetallic oxides can promote electron transfer through a unique adsorption mode and enhance the catalytic activity [9]. However, the catalytic degradation performance of the bimetallic oxide remains unsatisfactory because of the strong electronegativity of the O atom. The electrons of Co bonded with O are trapped by O atoms, resulting in a weak electronic interaction between PMS and the metal sites [10,11]. Thus, it is expected that replacing O with a

---

low-electronegativity atom, such as N, could enhance the interactions between PMS and metal sites, facilitating the cleavage of O-O bonds and the production of active species. To the best of our knowledge, metal nitrides have not been used as Fenton-like catalysts.

Herein, bimetallic metal nitride $NiCo_2N$ nanosheets (NS) with highly exposed marginal Co-N and Ni-N sites were synthesized by bonding Co and Ni with low- electronegativity N atoms. Their catalytic properties for pollutant degradation in Fenton-like processes were assessed for the first time. The main research objectives are as follows. First, assess the feasibility and catalytic activity of $NiCo_2N$ NS for PMS activation to degrade pollutants. Second, determine the important role of N in $NiCo_2N$ NS by comparing with $NiCo_2O_4$ NS. Third, clarify the active species generation mechanisms after the PMS molecule contacts the Co-N and Ni-N sites combining experiments and theoretical calculations. Finally, further elucidate the application potential of NiCo2N NS by analyzing its degradation performance in different water matrices.

2. Materials and methods

2.1. Synthesis and characterization of catalysts

The reagents used in this study are summarized in Text S1 of Supporting Information. The preparation of $NiCo_2N$ NS involved the synthesis of $Ni_{1/2}Co_{2/3}(OH)_2$ [9] and subsequent thermal treatment. First, $CoCl_2·6H_2O$, $NiCl_2·6H_2O$, and hexamethylene- tetramine with a molar ratio of 1:2:36 were dissolved in distilled water. Then, the mixture was refluxed at 95 °C for 5 h under stirring to obtain $Ni_{1/2}Co_{2/3}(OH)_2$, followed by heating at 350 °C for 2 h in NH_3 atmosphere in a tube furnace. Finally, the products were rinsed with distilled water and dried. For comparison, the control catalysts $NiCo_2O_4$ NS, Co_3N and Ni_3N were synthesized according to the preparation processes presented in Text S2. Characterization details for X-ray diffraction (XRD), scanning electron microscopy (SEM), atomic force microscopy (AFM), transmission electron microscopy (TEM) with energy-dispersive X-ray spectroscopy (EDS), N_2 adsorption/desorption experiments, X-ray photoelectron spectroscopy (XPS), Raman spectroscopy, zeta potential measurements, X-ray absorption near edge structure (XANES) and extended X-ray absorption fine structure (EXAFS) measurements are provided in Text S3.

2.2. Degradation experiments and analytical methods

The pollutant degradation experiments are described in Text S4. The norfloxacin (NOR) concentration was measured using high-performance liquid chromatography (HPLC, Persee L6, China) using an Agilent C18 column at a wavelength of 278 nm. A schematic of active species quenching experiments is presented in Text S5. Details of degradation kinetics analysis are presented in Text S6. D_2O was used to replace H_2O as the solvent to determine the role of $^1O_2$. The contributions of active species were calculated using the formula provided in Text S7. Effluents from a wastewater treatment plant (WWTP) were selected to test the practical application potential of the $NiCo_2N$ NS. The water quality parameters of the WWTP effluents are listed in Table S1. To study the effects of anions and dissolved organic compounds on the degradation, NaCl (10 mM), NaH_2PO_4 (10 mM), $NaNO_3$ (10 mM), $NaHCO_3$ (10 mM) and humic acid HA (50 mg/L) were added separately to the $NiCo_2N$ NS/ PMS degradation system. The applicability of $NiCo_2N$ NS was explored by evaluating the degradation of bisphenol A, rhodamine B, sulfamethoxazole and tetracycline. The concentrations of pollutants were detected by HPLC at wavelengths of 275, 550, 275, and 350 nm, respectively. The total organic carbon (TOC) was measured using a TOC analyzer (TOC-L, Shimadzu, Japan). For the cycling experiments, the spent $NiCo_2N$ NS catalyst was collected by filtration, rinsed with distilled water, and dried for the next round.

2.3. Calculations

Density functional theory (DFT) was applied using the Vienna Ab initio simulation package (VASP) for all theoretical calculations. Co_3N (space group: P6322) was selected as the basic model for $NiCo_2N$ calculations. The specific information is provided in Text S8.

3. Results and discussion

3.1. Characterizations of NiCo2N NS

During the preparation process (Fig. 1A), $NiCo_2N$ NS and $NiCo_2O_4$ NS (control sample) were obtained by annealing the hydroxide precursor in NH_3 and air, respectively. SEM (Fig. 1B and Fig. S1) and TEM (Fig. S2) images indicate that the $NiCo_2N$ and $NiCo_2O_4$ are ultra-thin two-dimensional nanosheets. Meanwhile, the $NiCo_2N$ NS has a flake-like morphology with more fractures and local aggregation (Fig. 1B and S2). The crystalline structures were confirmed via XRD (Fig. 1C). $NiCo_2O_4$ NS exhibited the characteristic peaks of $NiCo_2O_4$ at 31.2°, 36.7°, 44.6°, 55.4°, 59.1°, and 64.9°, attributed to the (220), (311), (400), (422), (511), and (440) planes of $NiCo_2O_4$, respectively. $NiCo_2N$ NS presented typical diffraction peaks at 38.6°, 41.8°, 44.3°, 58.1°, 70.0° and 77.6°, similar to Co_3N (39.1°, 41.6°, 44.4°, 58.1°, 70.7° and 77.7° in PDF Card No. 00-06-0691) and Ni_3N (38.9°, 42.1°, 44.5°, 58.5°, 70.6°, and 78.3° in PDF Card No. 00-10-0280). The diffraction peaks of Co_3N shifted after introducing Ni and similar results have been reported for $NiCo_2N$ and Co_3N nanosheets [12]. The lattice stripes with a spacing of 0.245 nm are ascribed to the exposed (111) facet of the $NiCo_2N$ NS (Fig. 1D). The uniform distributions of N, Co, and Ni in the EDS mapping diagrams (Fig. 1E) suggest the successful preparation of $NiCo_2N$ NS. The thickness of $NiCo_2N$ NS is 1.2–1.5 nm according to the AFM image (Fig. 1F). As shown in Fig. S3, $NiCo_2O_4$ NS has a larger surface area (102 m^2/g) than $NiCo_2N$ NS (31.6 m^2/g). Moreover, the N_2 adsorption-desorption curves of $NiCo_2N$ and $NiCo_2O_4$ exhibit typical H3 hysteresis loops, confirming the existence of slit pores derived from nanosheet accumulation.

The co-existence of Ni, Co, N, and O elements and the valence states in $NiCo_2N$ NS and $NiCo_2O_4$ NS were confirmed by their XPS survey spectra (Fig. S4). The high-resolution O 1 s spectra (Fig. 2A) can be fitted with three peaks at 532.1, 531.1, and 529.8 eV, ascribed to lattice oxygen [13], surface OH [14] and adsorbed H_2O [15,16], respectively. Compared to the XPS spectra of $NiCo_2O_4$ NS, the lattice oxygen in $NiCo_2N$ NS disappears because the O is replaced by N. The N 1 s spectrum (Fig. 2B) can be deconvoluted into four peaks. The more distinct peaks at 397.6 and 398.3 eV belong to Ni-N and Co-N [17,18], respectively, confirming the successful synthesis of $NiCo_2N$ NS. The peaks at 399.5 and 402.9 eV in the N 1 s spectrum are attributed to C-N and O-N, respectively [19,20]. The Co 2p spectrum of the $NiCo_2N$ NS (Fig. 2C) can be deconvoluted into two shake-up satellites (785.8 eV and 802.6 eV) and two spin-orbit doublets. The spin-orbit binary peaks are assigned to Co $2p_{1/2}$ (Co^{2+} for 796.9 eV and Co^{3+} for 794.2 eV) and Co $2p_{3/2}$ (Co^{2+} for 781.2 eV and Co^{3+} for 778.4 eV) [21,22]. In Fig. 2D, the spin-orbit doublets in Ni 2p spectrum are assigned to Ni $2p_{1/2}$ (Ni^{2+} for 870.3 eV and Ni^{3+} for 874.1 eV) and Ni $2p_{3/2}$ (Ni^{2+} for 854.5 eV and Ni^{3+} for 856.3 eV) [23,24]. According to the above XPS analysis, the content ratio of Co(II) is 15.6 % in $NiCo_2N$ NS, higher than that in $NiCo_2O_4$ NS, indicating that $NiCo_2N$ NS may possess better catalytic activity for PMS activation than $NiCo_2O_4$ NS.

The coordination environment and chemical states of the Co and Ni atoms in the $NiCo_2N$ and $NiCo_2O_4$ NS were explored using XANES and EXAFS. The normalized Co (Fig. 2E) and Ni k-edge XANES spectra (Fig. 2F) show that the absorption edge position of the $NiCo_2N$ NS is located between those of Co/Ni foil and CoO/NiO, suggesting that the oxidation states of the Co and Ni atoms are between M^0 and M^{2+}. The absorption edge of the $NiCo_2O_4$ NS is located on the right side of CoO/ NiO, suggesting that the oxidation states of the Co and Ni atoms are
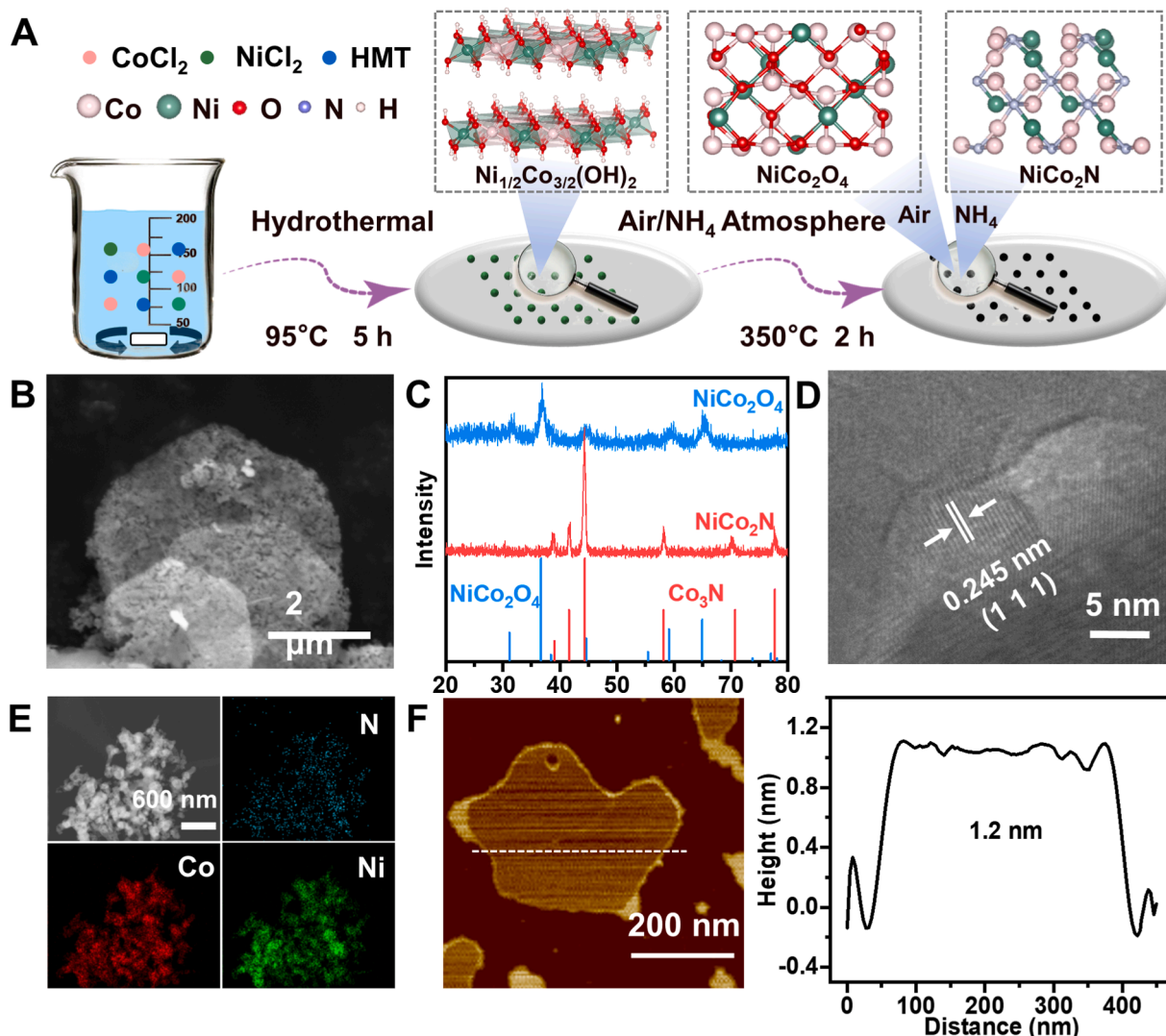
Fig. 1. (A) Schematic of the synthesis of NiCo$_2$N NS and NiCo$_2$O$_4$ NS. (B) SEM image of NiCo$_2$N NS. (C) XRD patterns of NiCo$_2$N NS and NiCo$_2$O$_4$ NS. (D) Lattice fringe. (E) EDS mapping of NiCo$_2$N NS. (F) AFM image of NiCo$_2$N NS.

higher than that of M^{2+}. The cation distribution in the spinel was evaluated using the Fourier transform (FT) of the EXAFS. For NiCo$_2$O$_4$ NS, the peak signals at 2.5 and 3 Å indicate that Co occupies both octahedral and tetrahedral sites. While the Ni K-edge EXAFS spectra (Fig. 2H) only show a peak at 2.5 Å, indicating that Ni only occupies octahedral sites. Therefore, the as-prepared NiCo$_2$O$_4$ NS is an inverse spinel, where the Co-occupying tetrahedral sites are bivalent, and the Co- and Ni-occupying octahedral sites are trivalent [9]. The Co K-edge EXAFS spectra (Fig. 2G) shows a prominent peak at approximately 1.26 Å, associated with the Co-N band. No significant Co-O bond peak is observed at 1.44 Å, indicating that the O atoms in NiCo$_2$N NS in the XPS spectrum (Fig. 2A) mainly originate from the surface-OH and adsorbed H$_2$O. In addition, the Co-Co/Ni bond of NiCo$_2$N NS is located at 2.24 Å (between Co foil and NiCo$_2$O$_4$ NS), indicating that Co-N bonds have a shorter electron transfer distance than Co-O bonds. The FT (Fig. 2H) of Ni K-edge EXAFS spectrum shows similar results, with peaks at 1.5 Å and 2.3 Å attributed to Ni-N and Ni-/NiCo bonds, respectively. Visualization for electronic and structural analysis was used to measure the bond lengths between atoms in the NiCo$_2$N NS and NiCo$_2$O$_4$ NS models (Fig. 2I). Compared with the FT of Co/Ni K-edge EXAFS spectra (Fig. 2G and Fig. 2H), the bond lengths of the models increased by 0.34–0.5 Å, suggesting that the bond lengths determined by EXAFS agree well with the theoretical calculation.

3.2. Performance of NiCo$_2$N NS for activating PMS to degrade NOR

To evaluate the catalytic activity of NiCo$_2$N NS for PMS activation, its degradation performance was studied in different systems with an initial NOR concentration of 20 mg/L. Distinctly, the degradation efficiency of NOR can reach 100 % within 10 min in the NiCo$_2$N NS/PMS system that 0.05 g/L of NiCo$_2$N NS and 1 mM of PMS co-exist. The concentration of released F$^-$ was also recorded (Fig. S5). When the initial concentration of NOR was 20 mg/L (0.06 mM), the concentration of released F$^-$ was increased during the degradation process and about 0.58 mg/L (0.03 mM) of F$^-$ was released within 10 min. This result is consistent with the TOC result that 49.89 % of NOR is mineralized (The TOC results are shown and discussed below). Meanwhile, the NOR degradation efficiency in the NiCo$_2$O$_4$ NS/PMS system is only 45.9 % within 10 min. NOR is hardly degraded in the PMS alone system without the addition of catalysts (Fig. 3A), indicating that the self-decomposition rate of PMS is considerably low. Moreover, the NOR removal efficiency is only 5.9 % in the presence of NiCo$_2$N NS and 12.7 % in the presence of NiCo$_2$O$_4$ NS without the addition of PMS, owing to surface adsorption (Fig. 3A). This result is consistent with their specific surface areas (Fig. S3).

The degradation rate constants (k) of the NiCo$_2$N NS/PMS/NOR system reaches 0.694 min^{-1}, which is 14.2 times higher than that of the NiCo$_2$O$_4$ NS/PMS/NOR system (0.048 min^{-1}) (Fig. 3B), indicating that
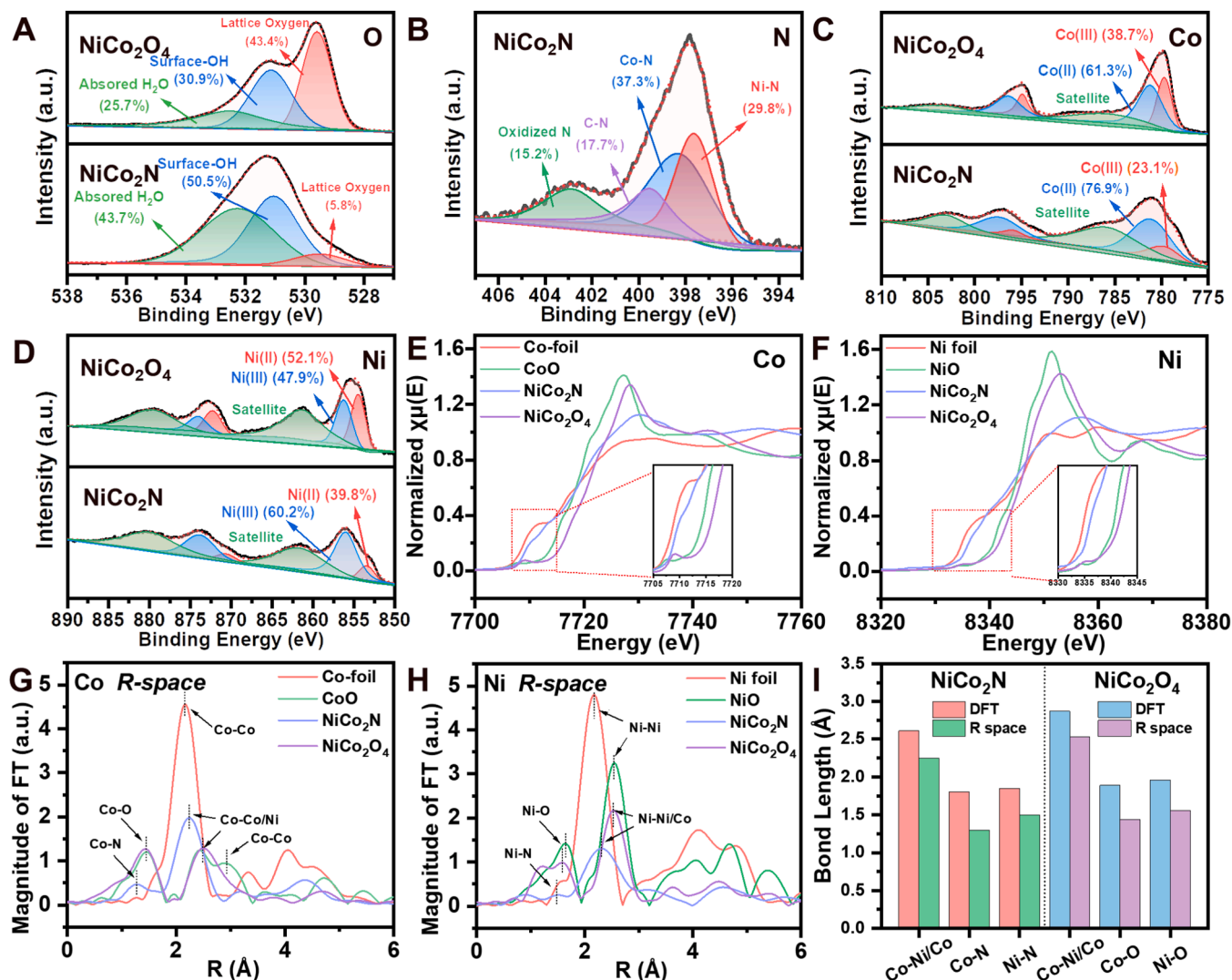
Fig. 2. XPS spectra of NiCo$_2$N NS and NiCo$_2$O$_4$ NS: (A) O 1 s; (B) N 1 s; (C) Co 2p; (D) Ni 2p. (E) Normalized XANES at the Co K-edge; (F) Normalized XANES at the Ni K-edge. (G) FT-EXAFS fitting curves at R space of Co K-edge. (H) FT-EXAFS fitting curves at R space of Ni K-edge for Co foil, CoO, NiCo$_2$N, and NiCo$_2$O$_4$. (I) Comparison of bond lengths of NiCo$_2$N and NiCo$_2$O$_4$ determined by XANES and DFT calculations.

the specific surface area of the material is not the main factor affecting its catalytic performance. Degradation of NOR by NiCo$_2$O$_4$ NS (0.05 mg/L) and NiCo$_2$N NS (0.065 mg/L) with the same Co content was compared (Fig. S6), confirming that NiCo$_2$N NS also has better catalytic performance than NiCo$_2$O$_4$ NS. PMS consumption also confirms the outstanding catalytic performance of NiCo$_2$N NS (Fig. S7). The degradation efficiencies of NOR in the NiCo$_2$N NS/PMS, Co$_3$N/PMS, and Ni$_3$N/PMS systems are much higher than those in their corresponding oxide/PMS systems, indicating that N atoms play a crucial role in PMS activation (Fig. 3A). Among the reported high-activity catalysts for NOR degradation listed in Fig. 3C and Table S2, such as bimetallic spinel oxides, carbon materials, calcite, and complex catalysts, NiCo$_2$N NS shows the highest kinetic rate, despite the lowest catalyst dosage (0.05 g/L) and the highest NOR concentration (20 mg/L).

The influence of the NiCo$_2$N NS dosage on NOR degradation was evaluated. When the concentration of NiCo$_2$N NS is 0.2 g/L, the degradation efficiency reaches 100 % within 5 min (Fig. 3D). With the concentration decreasing to 0.1 g/L and 0.05 g/L, NOR can still achieve 100 % degradation within 10 min Fig. 3D also shows that the k value decreases from 0.951 min^{-1} to 0.805 and 0.694 min^{-1} as the dosage decreases from 0.2 g/L to 0.1 and 0.05 g/L, respectively. Therefore, an excellent NOR degradation efficiency can be achieved when the NiCo$_2$N

NS concentration is as low as 0.05 g/L. The effect of PMS concentration on NOR degradation is shown in Fig. 3E. At a PMS concentration of 0.667 mM, the degradation efficiency reaches 96.1 % within 30 min. As the PMS concentration increases from 0.667 mM to 1 and 1.333 mM, the degradation efficiency remains 100 % within 10 min. Moreover, the actual extent of PMS consumption under the conditions used in Fig. 3E is shown in Fig. S8. PMS was depleted by NiCo$_2$N NS within 10 min at a PMS concentration of 0.667 mM. NOR degradation continued to increase possibly due to the surface adsorption of catalyst.

The effect of pH on NOR degradation in the NiCo$_2$N NS/PMS system is shown in Fig. 3F. At the initial pH values of 7, 9, and 11, 100 % degradation is achieved. At pH values of 3, 5, and 11, the degradation efficiencies are reduced to 84.5 %, 97.5 %, and 86.3 %, respectively, which may be related to the surface charge of NiCo$_2$N NS/NOR. With an isoelectric point of 6.3 (Fig. S9), the NiCo$_2$N NS is positively or negatively charged when the pH is lower or higher than 6.3. Considering the pK$_a$ values of NOR are 6.32 and 8.47 [25], NOR exists mainly as a cation (NOR$^+$) or anion (NOR$^-$) when the pH is lower than 6.32 or higher than 8.47 and as a zwitterionic form (NOR$^\pm$/NOR^0) when the pH is between 6.32 and 8.47. Therefore, when the initial pH is below 6.3 or above 8.47, both NOR and NiCo$_2$N NS are positively or negatively charged. Strong electrostatic repulsion can impede the adsorption of NOR on the active
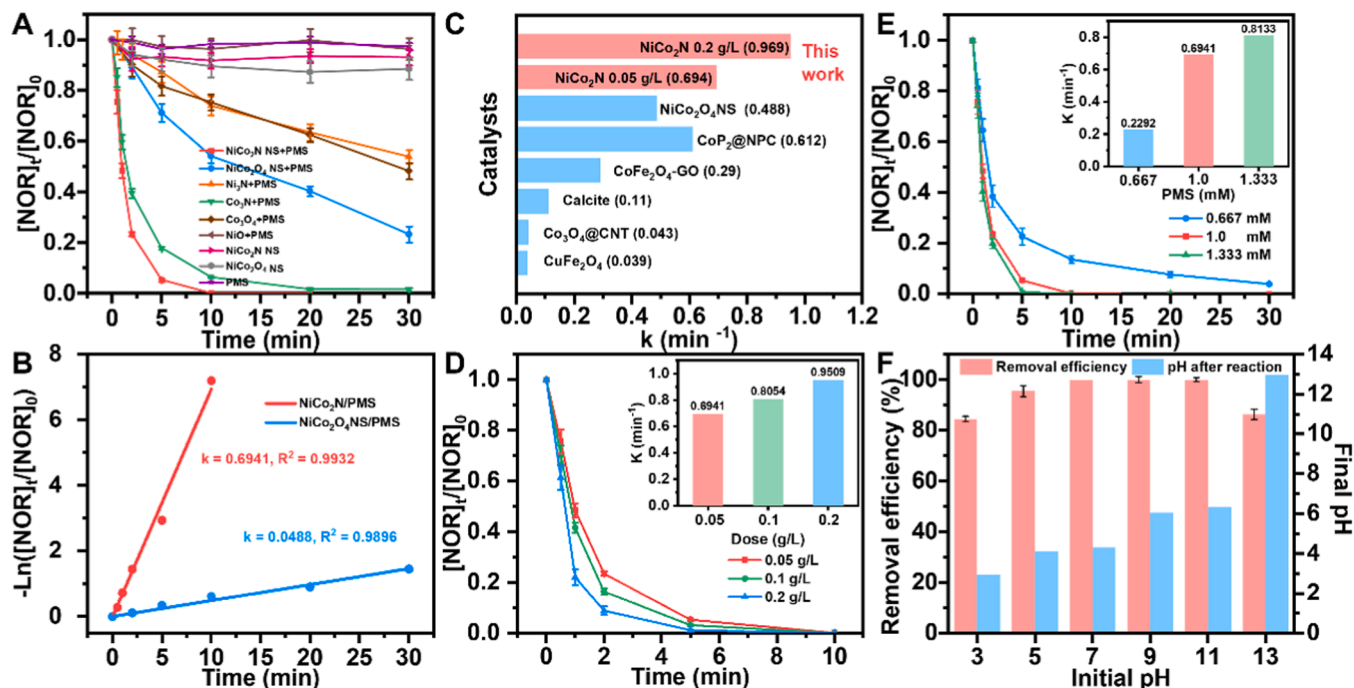
Fig. 3. NOR degradation by PMS activation catalyzed by $NiCo_2N$ NS and control catalysts. (A) NOR degradation performance. (B) Degradation rate constants (k) of $NiCo_2N$ NS and $NiCo_2O_4$ NS. (C) Comparison of k values of several catalysts for degradation of NOR. (D) Effect of $NiCo_2N$ NS dosage on NOR degradation. (E) Effect of PMS concentration on NOR degradation. (F) Effect of initial solution pH on NOR degradation. Experimental conditions unless otherwise specified: $[NOR]_0 = 20$ mg/L, $[PMS]_0 = 1$ mM, $[Catalyst] = 0.05$ g/L, 25 °C, pH = 7.0.

sites of the $NiCo_2N$ NS, decreasing the NOR degradation efficiency. When the initial pH is 1, the NOR degradation efficiency drops sharply to 12.92 %, owing to the complete dissolution of the $NiCo_2N$ NS. The pH

changes were measured in the $NiCo_2N$ NS systems after the addition of PMS. When the initial pH is 7, the pH decreases to approximately 3.4 and stabilizes after adding PMS (Fig. S10). Similarly, after
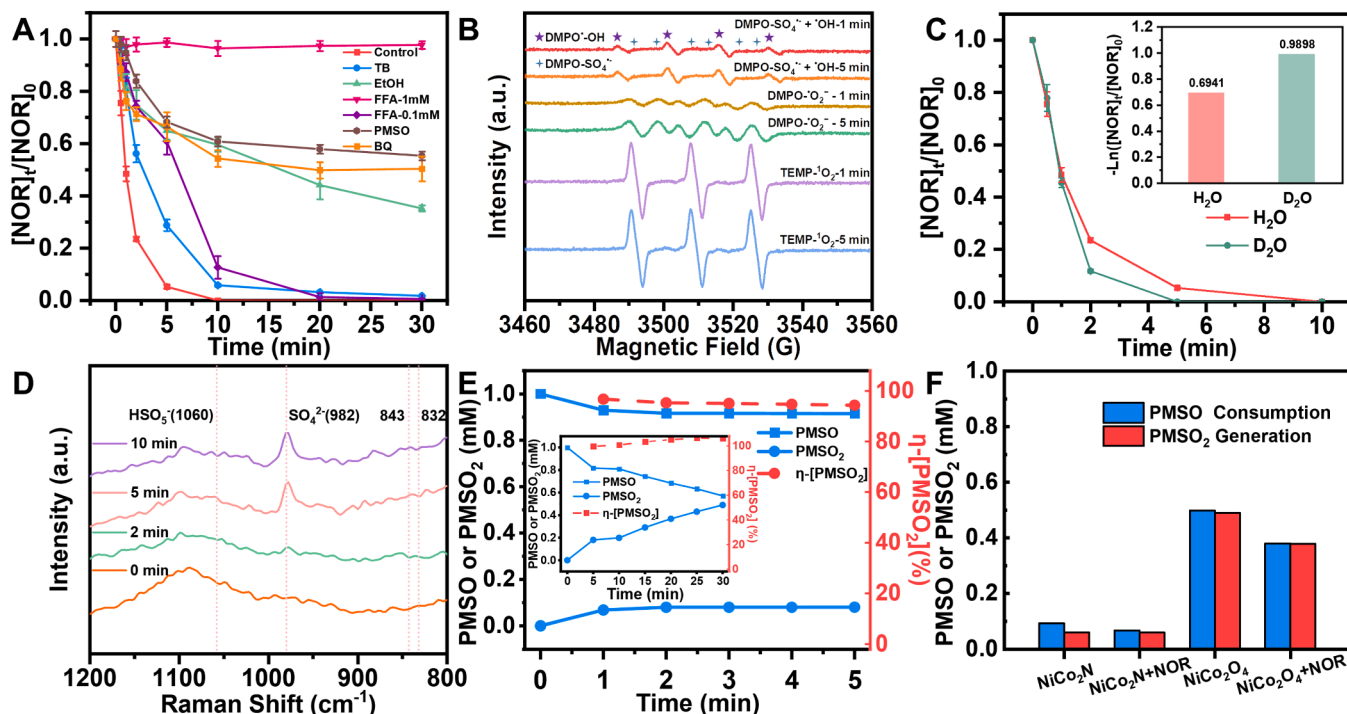

Fig. 4. (A) Quenching experiment, (B) EPR signals obtained with DMPO and TEMP as spin-trapping agents, (C) Degradation of NOR using H_2O or D_2O as a solvent in the $NiCo_2N$ NS/PMS system, (D) In situ Raman spectra collected at different reaction times in $NiCo_2N$ NS/PMS system. PMSO consumption, $PMSO_2$ generation, and $\eta PMSO_2$ (the ratio of generated $PMSO_2$ to consumed PMSO) with or without NOR in $NiCo_2N$ NS/PMS (E) and $NiCo_2O_4$ NS/PMS (F). Experiment conditions unless otherwise stated: $[NOR]_0 = 20$ mg/L, $[PMS]_0 = 1$ mM, $[TB] = [Ethanol] = 300$ mM, $[BQ] = 10$ mM, $[FFA] = 0.1$ and 1 mM, $[Catalysts] = 0.05$ g/L, 25 °C, pH = 7.0.

adding PMS at an initial pH of 5–11, the final pH stabilizes between 3.2 and 4.6. The decrease in pH after adding PMS is due to the released H^+, which is consistent with the results of theoretical calculations (H^+ was released during the $^1O_2$ generation process).

3.3. PMS activation mechanism and the role of N atoms

The XPS profiles of the $NiCo_2N$ NS after the catalytic reaction were also recorded. Elemental analyses before and after the reaction are presented in Table S3. The surface OH is consumed during the reaction (Fig. S11A), indicating a heterogeneous catalytic reaction on the surface. As shown in Fig. S11B, the attachment of the intermediate product of NOR to the $NiCo_2N$ NS causes a slight change in the ratio of O-N and C-N before and after the reaction. The change in the valence states of Co (Fig. 2C and S11C) and Ni (Fig. 2d and S11D) before and after the reaction indicates that electron transfer is involved in the catalysis. This coordination mode of Ni-N and Co-N can promote PMS activation by changing the electron distribution of the active sites [16,26].

The active species in the $NiCo_2N$ NS/PMS system were identified using free radical quenching experiments. Compared to the unquenched control, the degradation efficiency decreases by only 1.2 % within 30 min after adding tert-Butanol (TB) (Fig. 4A), indicating that $^•OH$ is not the main active species for NOR degradation. Meanwhile, the addition of ethanol (Fig. 4A), as a quencher of $^•OH$ and $SO_4^{•-}$ [27], inhibits the NOR degradation efficiency by 35.2 % within 30 min, suggesting that $SO_4^{•-}$ contributes significantly to NOR degradation. Furfuryl alcohol (FFA) is a $^1O_2$ quencher [14,28]. However, excessive FFA can react directly with PMS. Fig. S12 shows that the consumptions of PMS after the addition of FFA in the absence of catalyst at concentration of 0.1 and 1 mM are negligible. With the concentration of FFA increases from 0.1 to 1 mM, the NOR degradation efficiency decreases sharply from 99.4 % to 2.2 %. In Contrast, the inhibitory effect on the $NiCo_2O_4$ NS/PMS system is only 26.8 % when the FFA concentration is 1 mM (Fig. S13). These contrasting quenching experimental results confirm that $^1O_2$ plays an important role in the $NiCo_2N$ NS/PMS/NOR system. When benzoquinone (BQ), a scavenger of $^•O_2^-$ [29], is present in the $NiCo_2N$ NS/PMS system, the NOR degradation efficiency decreases to 50.2 % within 30 min (Fig. 4A). The $^1O_2$ can be generated from the self-decomposition of PMS or the conversion of $^•O_2^-$. Considering the extremely low self-decomposition rate of PMS (k = 4.7–5.9 $\times$ 10^{-2} $M^{-1}s^{-1}$ at pH = ~9–10) [30], $^1O_2$ is mainly produced by $^•O_2^-$ in the degradation process. Therefore, it is preliminarily concluded that $SO_4^{•-}$ and $^1O_2$ are the active species responsible for degrading NOR in the $NiCo_2N$ NS/PMS system.

To further confirm the contribution of different active species, the electron paramagnetic resonance (EPR) technique was employed to capture instantaneous active species [31]. 5,5-Dimethyl-1-pyrroline N-oxide (DMPO) was used as a quenching agent for $SO_4^{•-}$, $^•OH$, and $^•O_2^-$ in the $NiCo_2N$ NS/PMS system. The characteristic signal of DMPO-$SO_4^{•-}$ with the intensity of 1:1:1:1:1:1 emerges at 1 min (Fig. 4B) and does not change significantly after 5 min. The characteristic signal of DMPO–$^•O_2^-$ is also observed at 1 min, and its intensity increases slightly after 5 min. Moreover, a strong triple signal with an intensity of 1:1:1 belonging to TEMP-$^1O_2$ is observed after 1 min and remains unchanged after 5 min $^•OH$ can be produced from $SO_4^{•-}$-generating systems from weakly acidic to alkaline condition, resulting in the significant signal of DMPO-$^•OH$ and an unrecognizable signal of DMPO-$SO_4^{•-}$ [32]. This phenomenon is commonly occurred in PMS activation system [33–36]. Thus, EPR results are consistent with quenching experiments, confirming that $SO_4^{•-}$ and $^1O_2$ are the main active species for NOR degradation in the $NiCo_2N$ NS/PMS system. The use of D_2O as an alternative solvent accelerates NOR degradation (Fig. 4C), Moreover, the degradation rates of NOR in D_2O exhibit about 1.2 times higher than that in H_2O (Fig. S14), further verifying the contribution of $^1O_2$.

To analyze the chemical evolution of the $NiCo_2N$ NS during the activation of PMS, in situ Raman spectra of the $NiCo_2N$ NS interface were collected after adding PMS (Fig. 4D). The peak at 1060 cm^{-1} corresponds to the HSO_5^- in PMS, and the peak at 982 cm^{-1} is due to the symmetric tensile vibration of S=O bonds in SO_4^{2-} [37]. The peak at 982 cm^{-1} increases with time, while the characteristic peak at 1060 cm^{-1} is not distinct, suggesting that $NiCo_2N$ NS has excellent PMS activation performance. PMS molecules are broken instantaneously after contacting $NiCo_2N$ NS to generate $SO_4^{•-}$. This is consistent with the theoretical calculation results indicating no transient adsorption state between the $NiCo_2N$ NS and PMS (see below). Characteristic peaks at 832 cm^{-1} and 843 cm^{-1} are not observed, implying that no electron transfer is involved in the $NiCo_2N$ NS/PMS system [38]. High-valent metal oxo species can oxidize methylphenyl sulfoxide (PMSO) to produce methylphenyl sulfone (PMSO$_2$). The role of Co(IV)=O is explored through PMSO consumption and PMSO$_2$ production. Approximately 6 % and 50 % of PMSO$_2$ are formed in the $NiCo_2N$ NS/PMS and $NiCo_2O_4$ NS/PMS systems, respectively, accompanied by the consumption of PMSO (Fig. 4E and F). These results demonstrate the limited role of Co (IV)=O in the $NiCo_2N$ NS/PMS system. Overall, the relative contributions of $SO_4^{•-}$ and $^1O_2$ are 33.4 % and 64.8 %, respectively (The computation formula is shown in Text S7). Attached by $SO_4^{•-}$ and $^1O_2$, NOR was degraded through hydroxylation, ring opening reaction of piperazine ring and quinolone ring, decarboxylation and defluorination reactions (Fig. S15).

The bonding modes between PMS and the active sites on the $NiCo_2O_4$ and $NiCo_2N$ NS were determined to explore the structure–activity relationships. The PMS molecule tends to contact with the Co-N(O) and Ni-N(O) active sites of $NiCo_2N$ NS ($NiCo_2O_4$ NS). Twelve adsorption modes and their optimization configurations between PMS and $NiCo_2N$ NS are presented in Fig. S16, and the corresponding adsorption energies are displayed in Table S4. The mode 5 with the maximum adsorption energy is more likely to be occurred and used for the next calculations. Notably, the O-O bond adsorbed on the surface of $NiCo_2N$ NS is broken while the O-O bond on the surface of $NiCo_2O_4$ NS is not broken after structure optimization (Fig. 5A). This phenomenon suggests that the $NiCo_2N$ NS might have better PMS activation capacity than $NiCo_2O_4$ NS [39]. The charge density difference (Fig. 5A) shows that the O-O bond in PMS on the surface of the $NiCo_2N$ NS can obtain more electrons (1.63) than that of $NiCo_2O_4$ NS (0.73). Thus, the substitution of N for O can induce more electron transfer from the Co and Ni sites to PMS, contributing to the enhanced PMS activation through the breakage of the O-O bond.

The role of N was further verified by the partial density of states (PDOS) of the Co atoms (Fig. 5B). The N atom optimizes the bonding orbital distribution in the Co 3d orbital. The Co 3d orbital electrons in $NiCo_2O_4$ NS are dispersed and concentrated at 1.53 eV below the Fermi level, while the Co electrons in $NiCo_2N$ NS are mostly located at 1.36 eV below the Fermi level. The well-distributed electrons close to Fermi-level in $NiCo_2N$ NS are responsible for its high chemical reactivity with PMS. After the PMS molecule contacts with the active sites, the reactive intermediates and the corresponding energy profiles (Fig. 5C). Notably, PMS on the Co-N and Ni-N sites tends to accept more electrons, leading to rapid decomposition of PMS into *SO_4^- and *OH (I→II). This is consistent with the in-situ Raman results. Then, $SO_4^{•-}$ is generated along II→IV pathway. Meanwhile, the formed HO* is deprotonated into O* (consistent with the decreased pH after adding PMS), followed by reacting with another O* to generate $^1O_2$ through the I→II→V→VI→VII pathway. In addition, compared with the generation of $^1O_2$ after $SO_4^{•-}$ removal, the direct generation of $^1O_2$ (I→II→III→IV) requires lower energy. Therefore, the characterization and DFT calculations confirm that the main active species in the $NiCo_2N$ NS/PMS system are $^1O_2$.

3.4. Practical application of NiCo2N NS/PMS system

Practical applications of the $NiCo_2N$ NS/PMS system were analyzed. The cyclic experiment shown in Fig. 6A proves that the $NiCo_2N$ NS/PMS system can completely degrade NOR within 30 min of the third cycle. In the fourth cycle, 100 % degradation is achieved within 45 min. The XRD
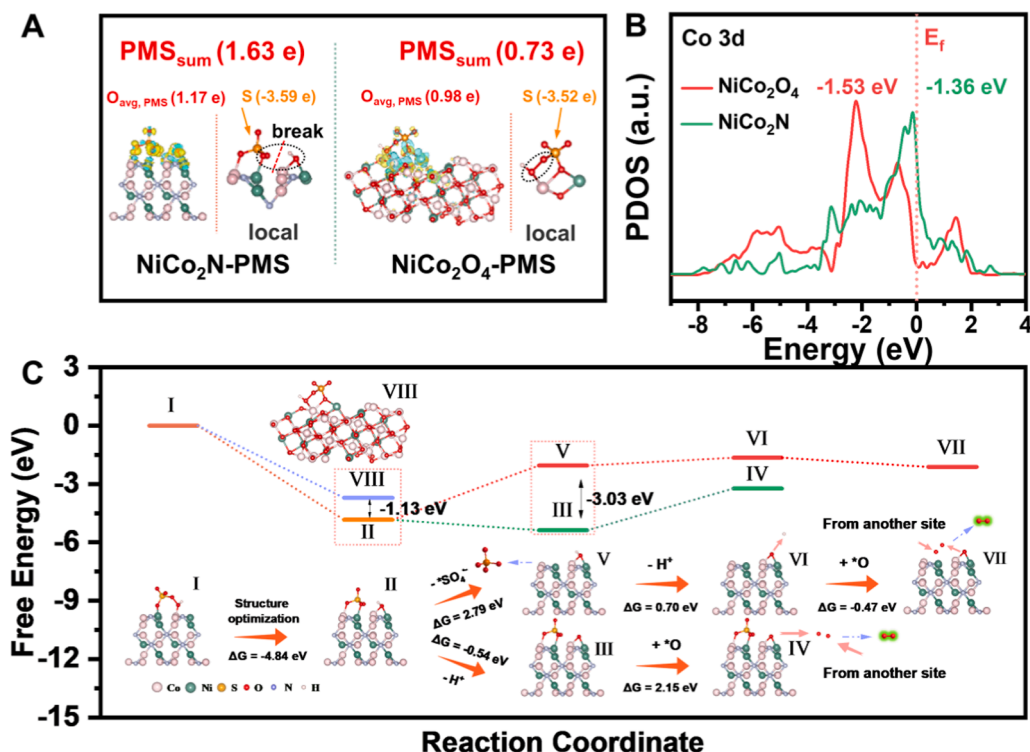
Fig. 5. (A) Charge density of PMS adsorption on NiCo$_2$N NS (left) and NiCo$_2$O$_4$ NS (right), in which the level of the isosurface is set to 0.006 e Å^{-3}. (B) PDOS of Co atom in NiCo$_2$O$_4$ NS and NiCo$_2$N NS. (C) Pathway and free energy of NiCo$_2$N NS to activate PMS and generate active species.
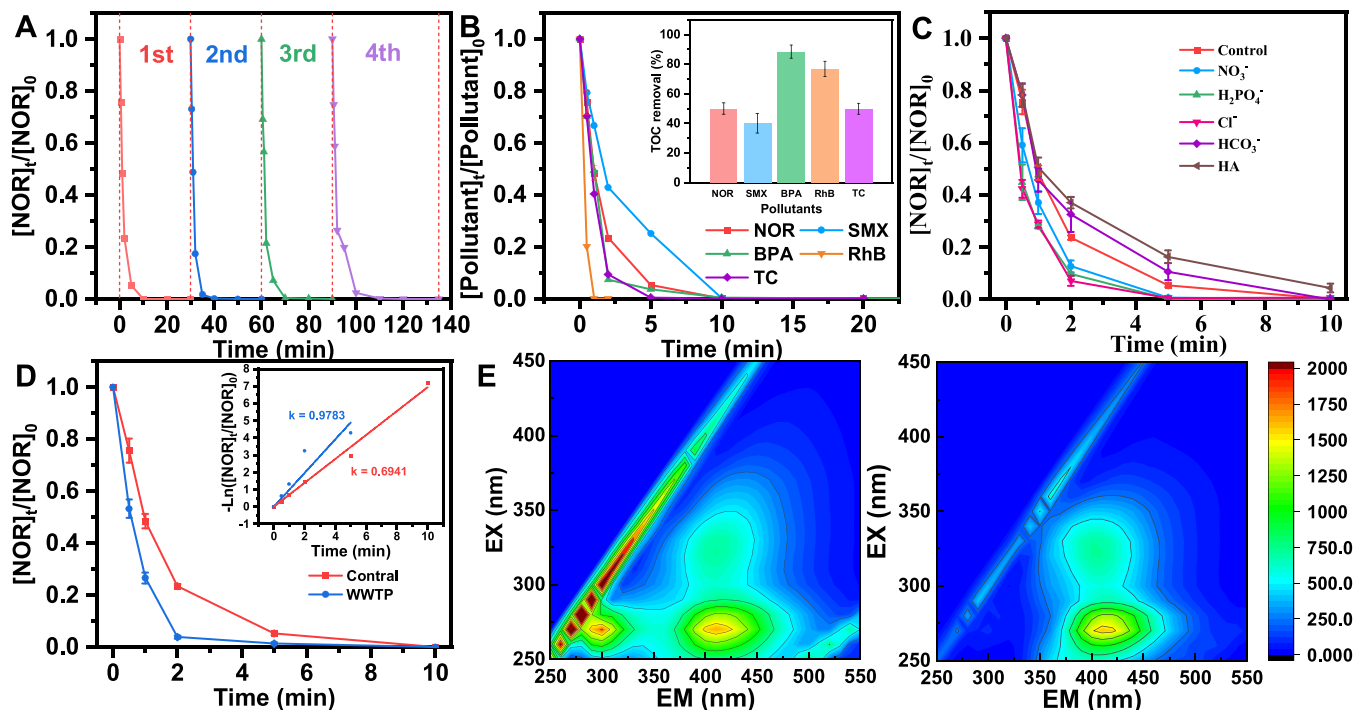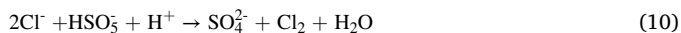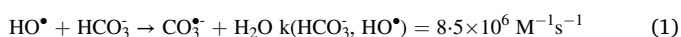

Fig. 6. (A) Cyclic experiment. (B) Degradation performance and TOC removal for different pollutants in NiCo$_2$N NS/PMS system. (C) Effect of anions on NOR degradation. (D) Comparison of NOR degradation efficiencies in WWTP effluents and deionized water. (E) 3D-EEM results of hospital wastewater before and after degradation. Experiment conditions: [Pollutant]$_0$ = 20 mg/L, [PMS]$_0$ = 1 mM, [NiCo$_2$N NS] = 0.05 g/L, [Cl$^-$] = [H$_2$PO$_4^-$] = [NO$_3^-$] = [HCO$_3^-$] = 10 mM, [HA] = 50 mg/L, 25 °C, pH = 7.0.

pattern (Fig. S17) of NiCo$_2$N NS after the reaction suggests that the crystalline structure of NiCo$_2$N NS remains unchanged after four cycles, confirming its stable structure. Moreover, after the first reaction, the concentrations of leaked Co^{2+} and Ni^{2+} are 0.53 mg/L and 0.05 mg/L in the NiCo$_2$N NS/PMS system, lower than those in the NiCo$_2$O$_4$ NS/PMS system (0.811 mg/L and 0.322 mg/L, respectively), further confirming

the stability of the $NiCo_2N$ catalyst (Fig. S18). Fig. 6B shows the removal ability of the $NiCo_2N$ NS/PMS system for different organic pollutants. The degradation of 20 mg/L of NOR (quinolones), sulfamethoxazole (sulfonamides), tetracyclines (tetracyclines), and bisphenol A (estrogen) reach 100 % within 10 min. Notably, rhodamine B is completely decolorized within 2 min. After 30 min, the TOC removal efficiencies are 49.89 %, 40.11 %, 88.32 %, 76.56 %, and 49.84 % for NOR, sulfamethoxazole, tetracyclines, bisphenol A, and rhodamine B, respectively.

The anion experiment (Fig. 6C) shows that HCO_3^- has an inhibitory effect on NOR degradation because $CO_3^{\bullet-}$ has lower activity than $SO_4^{\bullet-}$ (Eqs. 1 and 2) [40]. In the presence of $H_2PO_4^-$ and NO_3^-, PMS activation can be enhanced to promote NOR degradation. Cl^- is converted into $Cl^\bullet$ through Eq. 3 [41], followed by a chain reaction to generate HOCl and Cl_2 (Eqs. 4–8) [42,43]. The generated HOCl and Cl_2 react with HSO_5^- through charge transfer (Eqs. 9 and 10) to promote NOR degradation [44]. The existence of $H_2PO_4^-$ benefits the degradation process because that $H_2PO_4^-$ itself could active PMS activation to generate active species [45]. In addition to the inorganic ions, water often contains dissolved organic matter. When 50 mg/L of HA is present in the $NiCo_2N$ NS/PMS system, NOR degradation is inhibited because HA competes for the active species. Therefore, it is concluded that Cl^-, $H_2PO_4^-$, and NO_3^- can enhance the degradation performance of the $NiCo_2N$ NS/PMS system.

$$HO^\bullet + HCO_3^- \rightarrow CO_3^{\bullet-} + H_2O \quad k(HCO_3^-, HO^\bullet) = 8 \cdot 5 \times 10^6 \ M^{-1}s^{-1} \tag{1}$$

$$SO_4^{\bullet-} + HCO_3^- \rightarrow SO_4^{2-} + HCO_3^\bullet \quad k(HCO_3^-, SO_4^{\bullet-}) = 1 \cdot 6 \times 10^6 \ M^{-1}s^{-1} \tag{2}$$

$$SO_4^{\bullet-} + Cl^- \leftrightarrow SO_4^{2-} + Cl^\bullet \tag{3}$$

$$Cl^\bullet + Cl^- \leftrightarrow Cl_2^{\bullet-} \tag{4}$$

$$Cl^\bullet + Cl^\bullet \leftrightarrow Cl_2 \tag{5}$$

$$Cl_2^{\bullet-} + Cl_2^{\bullet-} \leftrightarrow Cl_2 + 2Cl^- \tag{6}$$

$$Cl_2^{\bullet-} + H_2O \leftrightarrow ClOH^{\bullet-} + H^+ + Cl^- \tag{7}$$

$$ClOH^{\bullet-} + H^+ \leftrightarrow Cl^\bullet + H_2O \tag{8}$$

$$Cl^- + HSO_5^- \rightarrow SO_4^{2-} + HOCl \tag{9}$$

$$2Cl^- + HSO_5^- + H^+ \rightarrow SO_4^{2-} + Cl_2 + H_2O \tag{10}$$

To evaluate the practical application of the $NiCo_2N$ NS/PMS system, the effluent from a WWTP containing inorganic ions and dissolved organic matter (Table S1) was selected as the experimental water. The chemical oxygen demand (9 mg/L), biochemical oxygen demand (44 mg/L), total nitrogen (6.38 mg/L), total phosphorus (0.11 mg/L), and suspended solid (8 mg/L) all meet the first-class A discharge standard of urban sewage treatment plants. The concentrations of chloride, bicarbonate, and sulfate were 273 mg/L, 220.08 mg/L, and 150 mg/L, respectively. The NOR degradation performance of the $NiCo_2N$ NS/PMS system in the WWTP effluent is shown in Fig. 6D, wherein 100 % NOR degradation efficiency is accomplished within 10 min. Furthermore, the k value of NOR degradation reached 0.9783 min^{-1} when the effluent from WWTP was employed as the solvent. The degradation in the WWTP effluent is faster than that in distilled water, attributed to the co-existence of anions.

Potential applications of the $NiCo_2N$ NS/PMS system were evaluated using actual hospital wastewater, which was used as the solvent to prepare a NOR solution with an initial concentration of 20 mg/L. The water quality parameters are presented in Fig. S19. The removal of NOR and organics ([$NiCo_2N$ NS] = 50 mg/L, [PMS] = 1 mM, pH = 6.2, T = 20 °C) was assessed by using three-dimensional excitation and emission matrix (3D-EEM) and UV scanning. The UV scanning results (Fig. S20) show that the peak in the range of 240–300 nm vanishes after treatment, proving the efficient degradation of contaminants. The fluorescence intensity (Fig. 6E) at approximately 300 nm in 3D-EEM decreases after treatment, indicating the removal of the corresponding organic matter. Thus, the $NiCo_2N$ NS/PMS system can efficiently eliminate NOR and other pollutants from hospital wastewater, confirming its great potential for practical applications.

4. Conclusions

This study reports the first use of transition-metal nitride ($NiCo_2N$) as a heterogeneous catalyst in PMS activation for contaminant degradation. The $NiCo_2N$ nanosheets showed high affinity toward PMS activation to oxidize different types of emerging contaminants, including norfloxacin, sulfamethoxazole, tetracyclines, rhodamine B, and bisphenol A. By using 20 mg/L of initial concentration, these pollutants could be completely degraded within 10 min with total organic carbon removal efficiencies of 40.11–88.32 %. During the PMS activation process, both Co-N and neighboring Ni-N sites synchronously contacted the same O atom in PMS through a "bridge" mode to transfer electrons. Compared with the Co-O and Ni-O sites in the $NiCo_2O_4$ NS, the Co-N and Ni-N active sites in the $NiCo_2N$ NS could transfer more electrons to accelerate the cleavage of the O-O bonds and generate more $SO_4^{\bullet-}$ and HO*. The formed HO* was then transformed into O*, followed by a reaction with another O* to generate $^1O_2$. The active species, $SO_4^{\bullet-}$ and $^1O_2$ were involved in pollutant degradation. The $NiCo_2N$ nanosheets maintained high catalytic activity and stability in a wide pH range and could effectively degrade NOR in complex effluents. Thus, this study demonstrated a promising PMS activation catalyst for practical applications and highlighted the significant role of N atoms in transition-metal catalyzed-PMS activation, providing an insightful reference for designing transition metal nitride-based catalysts.

CRediT authorship contribution statement

Pengcheng Cai: Methodology, Formal analysis, Investigation, Data curation, Writing - original draft, Visualization. **Xiaohui Zhang**: Data curation, Validation, Investigation. **Shuai Yang**: Conceptualization, Methodology, Validation, Investigation. **Hui Cui**: Data curation, Validation, Investigation. **Yonghao Wang**: Resources, Visualization. **Yaqi Huang**: Resources, Investigation. **Mengjie Qin**: Editing. **Dandan Han:** Resources, Investigation. **Xianfeng Yang**: Resources, Validation. **Peng Guo**: Resources, Validation. **Yuanyuan Sun**: Conceptualization, Supervision. **Dongjiang Yang**: Validation, Supervision.

Declaration of Competing Interest

The authors declare that they have no known competing financial interests or personal relationships that could have appeared to influence the work reported in this paper.

Data availability

Data will be made available on request.

Acknowledgements

Appendix A. Supporting information

Supplementary data associated with this article can be found in the online version at doi:10.1016/j.apcatb.2023.123446.

References

[1] K. Yin, Y. Shang, D. Chen, B. Gao, Q. Yue, X. Xu, Redox potentials of pollutants determining the dominate oxidation pathways in manganese single-atom catalyst (Mn-SAC)/peroxymonosulfate system: selective catalytic mechanisms for versatile pollutants, Appl. Catal. B-Environ. 338 (2023), 123029.

[2] Y.N. Shang, X. Xu, B.Y. Gao, S.B. Wang, X.G. Duan, Single-atom catalysis in advanced oxidation processes for environmental remediation, Chem. Soc. Rev. 50 (2021) 5281–5322.

[3] H. Dong, Y. Zou, K. Zhang, Y. Sun, B. Hui, D. Yang, L. Cai, J. Li, Biomimetic design of wood carbon-based heterogeneous catalysts for enhanced organic pollutants degradation, Chem. Eng. J. 451 (2023), 138568.

[4] C. Wang, X. Wang, H. Wang, L. Zhang, Y. Wang, C.-L. Dong, Y.-C. Huang, P. Guo, R. Cai, S.J. Haigh, X. Yang, Y. Sun, D. Yang, Low-coordinated Co-N₃ sites induce peroxymonosulfate activation for norfloxacin degradation via high-valent cobalt-oxo species and electron transfer, J. Hazard. Mater. 455 (2023), 131622.

[5] W.D. Oh, Z.L. Dong, T.T. Lim, Generation of sulfate radical through hetero-geneous catalysis for organic contaminants removal: current development, challenges and prospects, Appl. Catal. B-Environ. 194 (2016) 169–201.

[6] M. Yang, Z. Hou, X. Zhang, B. Gao, Y. Li, Y. Shang, Q. Yue, X. Duan, X. Xu, Unveiling the origins of selective oxidation in single-atom catalysis via Co-N₄-C intensified radical and nonradical pathways, Environ. Sci. Technol. 56 (2022) 11635–11645.

[7] S. Pang, C. Zhou, Y. Sun, K. Zhang, W. Ye, X. Zhao, L. Cai, B. Hui, Natural wood-derived charcoal embedded with bimetallic iron/cobalt sites to promote ciprofloxacin degradation, J. Clean. Prod. 414 (2023), 137569.

[8] G.P. Anipsitakis, D.D. Dionysiou, Radical generation by the interaction of transition metals with common oxidants, Environ. Sci. Technol. 38 (2004) 3705–3712.

[9] P.C. Cai, J. Zhao, X.H. Zhang, T.Y. Zhang, G.M. Yin, S. Chen, C. Dong, Y. Huang, Y. Y. Sun, D.J. Yang, B.S. Xing, Synergy between cobalt and nickel on NiCo₂O₄ nanosheets promotes peroxymonosulfate activation for efficient norfloxacin degradation, Appl. Catal. B-Environ. 306 (2022), 121091.

[10] Q.-Y. Wu, Z.-W. Yang, Z.-W. Wang, W.-L. Wang, Oxygen doping of cobalt-single-atom coordination enhances peroxymonosulfate activation and high-valent cobalt-oxo species formation, PANS 120 (2023), e2219923120.

[11] Z.-Y. Guo, C.-X. Li, M. Gao, X. Han, Y.-J. Zhang, W.-J. Zhang, W.-W. Li, Mn-O covalency governs the intrinsic activity of Co-Mn spinel oxides for boosted peroxymonosulfate activation, Angew. Chem. Int. Ed. 60 (2021) 274–280.

[12] X. Liu, W. Zang, C. Guan, L. Zhang, Y. Qian, A.M. Elshahawy, D. Zhao, S. J. Pennycook, J. Wang, Ni-doped cobalt-cobalt nitride heterostructure arrays for high-power supercapacitors, ACS Energy Lett. 3 (2018) 2462–2469.

[13] L. Qian, L. Gu, L. Yang, H.Y. Yuan, D. Xiao, Direct growth of NiCo₂O₄ nanostructures on conductive substrates with enhanced electrocatalytic activity and stability for methanol oxidation, Nanoscale 5 (2013) 7388–7396.

[14] J. Balamurugan, T.T. Nguyen, V. Aravindan, N.H. Kim, J.H. Lee, Flexible solid-state asymmetric supercapacitors based on nitrogen-doped graphene encapsulated ternary metal-nitrides with ultralong cycle life, Adv. Funct. Mater. 28 (2018), 1804663.

[15] P. Hu, M. Long, Cobalt-catalyzed sulfate radical-based advanced oxidation: a review on heterogeneous catalysts and applications, Appl. Catal. B-Environ. 186 (2016) 103–117.

[16] J. Ji, C. Zhang, X. Yang, F. Kong, C. Wu, H. Duan, D. Yang, Pt-stabilized electron-rich Ir structures for low temperature methane combustion with enhanced sulfur-resistance, Chem. Eng. J. 466 (2023), 143044.

[17] R. Zou, M. Xu, S.-A. He, X. Han, R. Lin, Z. Cui, G. He, D.J.L. Brett, Z.X. Guo, J. Hu, I. P. Parkin, Cobalt nickel nitride coated by a thin carbon layer anchoring on nitrogen-doped carbon nanotube anodes for high-performance lithium-ion batteries, J. Mater. Chem. A 6 (2018) 19853.

[18] P. Wang, J. Bai, K. Li, H. Ma, W. Li, X. Zhu, Y. Sun, B. Zhao, NiCo₂N hollow sphere with interconnected nanosheets shell: a potential anode material for high performance lithium-ion batteries, Chem. Eng. J. 425 (2021), 130607.

[19] K. Yoon, K. Shin, J. Park, S. Cho, C. Kim, J. Jung, J.Y. Cheong, H.R. Byon, H.M. Lee, I. Kim, Brush-like cobalt nitride anchored carbon nanofiber membrane: current collector-catalyst integrated cathode for long cycle Li-O₂ batteries, ACS Nano 12 (2018) 128–139.

[20] L.M. Yang, W.D. Chen, C.H. Sheng, H.L. Wu, N.T. Mao, H. Zhang, Fe/N-codoped carbocatalysts loaded on carbon cloth (CC) for activating peroxymonosulfate (PMS) to degrade methyl orange dyes, Appl. Surf. Sci. 549 (2021), 149300.

[21] C.S. Bao, J. Zhao, Y.Y. Sun, X.L. Zhao, X.H. Zhang, Y.K. Zhu, X.L. She, D.J. Yang, B. S. Xing, Enhanced degradation of norfloxacin by Ce-mediated Fe-MIL-101: catalytic mechanism, degradation pathways, and potential applications in wastewater treatment, Environ. Sci. -Nano 8 (2021) 2347–2359.

[22] Y. Gao, Q. Wang, G.Z. Ji, A.M. Li, Degradation of antibiotic pollutants by persulfate activated with various carbon materials, Chem. Eng. J. 429 (2022), 132387.

[23] H.L. Wang, C.B. Holt, Z. Li, X. Tan, B. Amirkhiz, Z. Xu, B. Olsen, T. Stephenson, D. Mitlin, Graphene-nickel cobaltite nanocomposite asymmetrical supercapacitor with commercial level mass loading, Nano Res. 5 (2012) 605.

[24] F.X. Ma, L. Yu, C.Y. Xu, X.W. Lou, Self-supported formation of hierarchical NiCo₂O₄ tetragonal microtubes with enhanced electrochemical properties, Energy Environ. Sci. 9 (2016) 862.

[25] C.J. Liang, Z.S. Wang, C.J. Bruell, Influence of pH on persulfate oxidation of TCE at ambient temperatures, Chemosphere 66 (2007) 106–113.

[26] C. Bao, H. Wang, C. Wang, X. Zhang, X. Zhao, C.-L. Dong, Y.-C. Huang, S. Chen, P. Guo, X. She, Y. Sun, D. Yang, Cooperation of oxygen vacancy and Fe^{III}/Fe^{II} sites in H₂-reduced Fe-MIL-101 for enhanced Fenton-like degradation of organic pollutants, J. Hazard. Mater. 441 (2023), 129922.

[27] Y. Zhao, M. Sun, Y. Zhao, L. Wang, D. Lu, J. Ma, Electrified ceramic membrane actuates non-radical mediated peroxymonosulfate activation for highly efficient water decontamination, Water Res. 225 (2022), 119140.

[28] F. Wilkinson, W.P. Helman, A.B. Ross, Rate constants for the decay and reactions of the lowest electronically excited singlet state of molecular oxygen in solution- an expanded and revised compilation, J. Phys. Chem. Ref. Data 24 (1995) 663–1021.

[29] P. Xu, S. Xie, X. Liu, L. Wang, X. Jia, C. Yang, Electrochemical enhanced heterogenous activation of peroxymonosulfate using CuFe₂O₄ particle electrodes for the degradation of diclofenac, Chem. Eng. J. 446 (2022), 136941.

[30] Y. Zhou, J. Jiang, Y. Gao, S.Y. Pang, Y. Yang, J. Ma, J. Gu, J. Li, Z. Wang, L. H. Wang, L.P. Yuan, Y. Yang, Activation of peroxymonosulfate by phenols: Important role of quinone intermediates and involvement of singlet oxygen, Water Res. 125 (2017) 209–218.

[31] P. Bilski, M. Reszka, M. Bilska, C.F. Chignell, Oxidation of the spin trap 5,5-dimethyl-1-pyrrolineN-oxide by singlet oxygen in aqueous solution, J. Am. Chem. Soc. 118 (1996) 1330–1338.

[32] H.-Y. Gao, C.-H. Huang, L. Mao, B. Shao, J. Shao, Z.-Y. Yan, M. Tang, B.-Z. Zhu, First Direct and unequivocal electron spin resonance spin-trapping evidence for pH-dependent production of hydroxyl radicals from sulfate radicals, Environ. Sci. Technol. 54 (2020) 14046–14056.

[33] G. Fang, T. Zhang, H. Cui, D.D. Dionysiou, C. Liu, J. Gao, Y. Wang, D. Zhou, Synergy between iron and selenide on FeSe₂(111) surface driving peroxymonosulfate activation for efficient degradation of pollutants, Environ. Sci. Technol. 54 (2020) 15489–15498.

[34] C. Chen, M. Yan, Y. Li, Y. Hu, J. Chen, S. Wang, X.-L. Wu, X. Duan, Single-atom Co sites confined in layered double hydroxide for selective generation of surface-bound radicals via peroxymonosulfate activation, Appl. Catal. B-Environ. 340 (2024), 123218.

[35] G.X. Huang, C.Y. Wang, C.W. Yang, P.C. Guo, H.Q. Yu, Degradation of bisphenol A by peroxymonosulfate catalytically activated with Mn₁.₈Fe₁.₂O₄ nanospheres: synergism between Mn and Fe, Environ. Sci. Technol. 51 (2017) 12611–12618.

[36] H.Y. Gao, C.H. Huang, L. Mao, B. Shao, J. Shao, Z.Y. Yan, M. Tang, B.Z. Zhu, First direct and unequivocal electron spin resonance spin-trapping evidence for pH-dependent production of hydroxyl radicals from sulfate radicals, Environ. Sci. Technol. 54 (2020) 14046–14056.

[37] T. Zhang, H.B. Zhu, J.-P. Croué, Production of sulfate radical from peroxymono-sulfate induced by a magnetically separable CuFe₂O₄ spinel in water: efficiency, stability, and mechanism, Environ. Sci. Technol. 47 (2013) 2784–2791.

[38] J.R. Yang, P. Li, X.G. Duan, D.Q. Zeng, Z.B. Ma, S.R. An, L.Q. Dong, W.L. Cen, Y. L. He, Insights into the role of dual reaction sites for single Ni atom Fenton-like catalyst towards degradation of various organic contaminants, J. Hazard. Mater. 430 (2022), 128463.

[39] F. Chen, L.-L. Liu, J.-J. Chen, W.-W. Li, Y.-P. Chen, Y.-J. Zhang, J.-H. Wu, S.-C. Mei, Q. Yang, H.-Q. Yu, Efficient decontamination of organic pollutants under high salinity conditions by a nonradical peroxymonosulfate activation system, Water Res. 191 (2021), 116799.

[40] X. He, K.E. O'Shea, Selective oxidation of H1-antihistamines by unactivated peroxymonosulfate (PMS): Influence of inorganic anions and organic compounds, Water Res. 186 (2020), 116401.

[41] R.X. Yuan, S.N. Ramjaun, Z.H. Wang, J.S. Liu, Effects of chloride ion on degradation of Acid Orange 7 by sulfate radical-based advanced oxidation process: implications for formation of chlorinated aromatic compounds, J. Hazard. Mater. 196 (2011) 173–179.

[42] G.P. Anipsitakis, T.P. Tufano, D.D. Dionysiou, Chemical and microbial decontamination of pool water using activated potassium peroxymonosulfate, Water Res. 42 (2008) 2899–2910.

[43] L.J. Peng, X.G. Duan, Y.N. Shang, B.Y. Gao, X. Xu, Engineered carbon supported single iron atom sites and iron clusters from Fe-rich Enteromorpha for Fenton-like reactions via nonradical pathways, Appl. Catal. B-Environ. 287 (2021), 119963.

[44] D.G.J. Larsson, C. Pedro, N. Paxeus, Effluent from drug manufactures contains extremely high levels of pharmaceuticals, J. Hazard. Mater. 148 (2007) 751–755.

[45] J. Ren, Y. Huang, J. Yao, S. Zheng, Y. Zhao, Y. Hou, B. Yang, L. Lei, Z. Li, D. D. Dionysiou, The role of reactive phosphate species in the abatement of micropollutants by activated peroxymonosulfate in the treatment of phosphate-rich wastewater, Water Res. 243 (2023), 120341.